Biophysical Journal
Article

Biophysical Society

Lipid membrane mimetics and oligomerization tune functional properties of proteorhodopsin

Chung-Ta Han,[1] Khanh Dinh Quoc Nguyen,[2] Maxwell W. Berkow,[1] Sunyia Hussain,[1] Ahmad Kiani,[3] Maia Kinnebrew,[4] Matthew N. Idso,[1] Naomi Baxter,[2] Evelyn Chang,[2] Emily Aye,[2] Elsa Winslow,[2] Mohammad Rahman,[3] Susanna Seppälä,[1] Michelle A. O'Malley,[1] Bradley F. Chmelka,[1] Blake Mertz,[3] and Songi Han[1,2,*]

[1]Department of Chemical Engineering, University of California, Santa Barbara, Santa Barbara, California; [2]Department of Chemistry and Biochemistry, University of California, Santa Barbara, Santa Barbara, California; [3]C. Eugene Bennett Department of Chemistry, West Virginia University, Morgantown, West Virginia; and [4]College of Creative Studies, Biology Department, University of California, Santa Barbara, Santa Barbara, California

ABSTRACT The functional properties of proteorhodopsin (PR) have been found to be strongly modulated by oligomeric distributions and lipid membrane mimetics. This study aims to distinguish and explain their effects by investigating how oligomer formation impacts PR's function of proton transport in lipid-based membrane mimetic environments. We find that PR forms stable hexamers and pentamers in both *E. coli* membranes and synthetic liposomes. Compared with the monomers, the photocycle kinetics of PR oligomers is ~2 and ~4.5 times slower for transitions between the *K* and *M* and the *M* and *N* photointermediates, respectively, indicating that oligomerization significantly slows PR's rate of proton transport in liposomes. In contrast, the apparent pKa of the key proton acceptor residue D97 (pKa_{D97}) of liposome-embedded PR persists at 6.2–6.6, regardless of cross-protomer modulation of D97, suggesting that the liposome environment helps maintain PR's functional activity at neutral pH. By comparison, when extracted directly from *E. coli* membranes into styrene-maleic acid lipid particles, the pKa_{D97} of monomer-enriched E50Q PR drastically increases to 8.9, implying that there is a very low active PR population at neutral pH to engage in PR's photocycle. These findings demonstrate that oligomerization impacts PR's photocycle kinetics, while lipid-based membrane mimetics strongly affect PR's active population via different mechanisms.

SIGNIFICANCE Transmembrane proteins play critical roles in a wide array of biological processes at the interface between the cell and its surrounding environment. The functional properties of these proteins have been shown to strongly depend on their oligomeric distributions and the membrane mimetic environment in which they are encapsulated. This study seeks to distinguish and compare the impacts of these two factors on the functional properties of a model transmembrane protein, the bacterial proteorhodopsin (PR). The findings from this study demonstrate the different mechanisms by which oligomerization and biomimetic composition modulate PR functions, emphasizing the importance of investigating the structure-function relationships of transmembrane proteins, while controlling for oligomerization and in different membrane mimetics.

INTRODUCTION

Transmembrane proteins are biomacromolecules that serve a multitude of crucial roles at the interface between the cell and its environment, including sensing (1) catalysis (2,3), and transport (4–6). These proteins have extensive hydrophobic regions, which facilitate interprotein interactions and require encapsulation in membrane mimetics, the former resulting in oligomerization (7–10). Both oligomer formation (9–17) and the choice of the membrane mimetic environment (18–25) can have significant impacts on the functional properties of these proteins. Since these two factors are often interdependent (11,13,21), few studies have distinguished and compared their effects on transmembrane protein function. We hypothesized that the effect of these factors can be delineated by studying proteorhodopsin (PR), a model transmembrane proton pump whose

Submitted December 21, 2021, and accepted for publication November 7, 2022.

*Correspondence: songi@chem.ucsb.edu

Chung-Ta Han, Khanh Dinh Quoc Nguyen and Maxwell W. Berkow contributed equally to this work.

Editor: Charles Deber.

https://doi.org/10.1016/j.bpj.2022.11.012

functional properties can be measured as a function of systematic modulation of the extent of oligomerization (11) or the makeup of the biomimetic environment (18–21).

PR is a light-driven proton pump that is found in a variety of marine bacteria. The minimal functional unit of PR is a polypeptide chain that transverses the bacterial plasma membrane seven times, and that binds a retinal chromophore. PR is readily expressed in heterologous systems and known to form functional oligomers (primarily pentamers and hexamers) in a wide variety of membrane mimetic environments, including micellar (21), bicellar (18–20), and nanodisc systems (26). PR's proton transport properties are conveniently assessed by optical absorption of the embedded retinal to evaluate: 1) the rate of proton transport and 2) the population of PR's active state. i) The rate of proton transport of PR is measured by the time-resolved change in optical absorbance after excitation with a pulsed green laser (27–29). Photoactivated PR undergoes a series of conformational changes that perturb the local environment of the retinal chromophore, resulting in photointermediates that constitute the photochemical reaction cycle. The transient conformational states, sequentially labeled as K, M_1/M_2, N, and PR', contribute to the overall optical absorbance spectrum, with partially resolved absorbances centered respectively at 555, 410, 560, and 520 nm. ii) The activity of PR depends on the protonation state of its primary proton acceptor residue D97, i.e., pKa_{D97} (29–32). Light-induced isomerization of the embedded retinal enables proton transfer to residue D97, requiring the aspartic acid to be deprotonated in the ground state (31). The active form of PR, when residue D97 is deprotonated, absorbs maximally at around 518 nm, exhibiting a pink color. Conversely, when D97 is protonated and therefore unavailable to accept protons, PR absorbs maximally at around 535 nm, exhibiting a purple color. Given this pH-dependent color transition, the pKa_{D97} of PR, i.e., the active state of PR, can be readily observed via optical absorption spectroscopy as a function of bulk solution pH, followed by determination of the isosbestic point at 570 nm (29,32,33).

Using these well-established approaches, previous studies found that detergent-solubilized PR is affected more strongly by oligomeric distribution than by detergent micelle composition (10,11,21). For example, PR's photocycle kinetics in detergent micelles are only subtly modulated by varying micelle composition, though are significantly slowed down by oligomerization (21). Furthermore, oligomerization is crucial for maintaining the population of active PR at neutral pH, given that the pKa_{D97} of PR oligomers (6.5–6.7) is much lower than that of its monomeric form (7.4–7.8) regardless of detergent type (11). In contrast, it has been found that liposome composition strongly influences PR's proton transport properties. Specifically, the apparent pKa_{D97} of PR in positively charged POPC/DOTAP liposomes (with 5.6) has been shown to be much lower than in the negatively charged POPC/POPG counterpart (with 7.6), while in the presence of 150 mM NaCl concentration, these differences are smaller (20). Clearly, both oligomer distribution and lipid-based mimetic composition can impact PR's proton transport properties. However, it is unclear which factor plays a stronger role and by what mechanism.

It is clear that the cross-protomer W34-H75 hydrogen bond stabilizes the protonated state of residue D97, even though it remains unclear how oligomerization affects the overall proton transport function of PR (34–37). The functional role of PR oligomerization can be investigated by disrupting cross-protomer interactions and observing changes in PR's proton transport properties. PR oligomers can be disrupted and separated by amino acid substitutions or by size-exclusion chromatography (SEC). The W34D substitution disrupts the cross-protomer hydrogen bond while maintaining the PR oligomer assemblies, and leads to a substantially increased pKa_{D97} (34,36). The E50Q substitution also disrupts the cross-protomer interaction, but by destabilizing the PR oligomers given that residue E50 is among the key residues at the oligomeric interface of PR (36). Finally, SEC can be used to isolate the smaller oligomeric species of PR wild-type (WT) that coexist with the larger (pentamer and hexamer) oligomer populations.

In this study, we characterize the functional roles of PR oligomerization in different lipid-based membrane mimetic platforms, including synthetic POPC/POPG liposomes and styrene maleic acid (SMA) lipid particles (SMALPs). The oligomeric distributions of PR in *E. coli* membranes and liposomes are investigated by chemical cross-linking and gel electrophoresis, electron paramagnetic resonance (EPR) spectroscopy, and molecular dynamics (MD) simulations. The proton transport function of the W34D mutant, E50Q mutant, and various SEC-separated oligomeric species of PR WT was evaluated via measurements of pKa_{D97} and photocycle kinetics. The novel findings from this study highlight the substantial impact of oligomeric distribution and lipid-based membrane mimetics on the function of PR.

MATERIALS AND METHODS

PR expression, purification, and separation of oligomers

Cysteine-free green-light absorbing PR with a C-terminal 6× His tag, both with and without the E50Q mutant that increased the population of monomeric PR (36) and the W34D mutant that disrupted the cross-protomer interaction (34), were expressed and purified using the protocol described in our previous studies (10,11). In brief, site-directed mutagenesis with a two-stage polymerase chain reaction technique (38) was applied here to introduce desired single mutations at residues mentioned above. The PR gene template with desired mutations was then cloned into a pET26b (+) vector (Novagen, Burlington, MA, USA) for expression in BL21(DE3). After PR was expressed and then purified by first isolating membranes using centrifugation, solubilizing membrane proteins in 2 wt % DDM, and then using Ni-NTA resin (Thermo Scientific, Waltham, MA, USA) in batch mode to pull down His-tagged PR, the protein was buffer exchanged into a 150 mM potassium chloride, 50 mM potassium phosphate dibasic buffer (pH 8.2) with 0.05 wt % DDM using a PD-10 desalting column contains

Sephadex G-25 resin (GE Healthcare, Chicago, IL, USA) for storage and characterization purposes.

The removal of His-tag was done using a tobacco etch virus (TEV) protease (Sigma Aldrich, Burlington, MA, USA), which recognize and cleave the sequence ENLYFQS in between the C-terminus of PR and the His-tag. His-tag removal reaction was done by first buffer exchanging PR into a 50 mM Tris-HCl buffer (pH 8) with 0.5 μM EDTA, 1 mM DTT, and 0.05 wt % DDM after its elution from Ni-NTA resin. Next, TEV protease was added to the PR solution at a protein-to-protein ratio of 1:100 (w/w) and incubated overnight at 4°C with gently mixing. The reacted solution was then buffer exchanged into the 50 mM potassium phosphate dibasic buffer (pH 8.2) with 150 mM potassium chloride and 0.05 wt % DDM using the PD-10 desalting column for removing the EDTA, and then combined with the Ni-NTA resin. The mixture was mixed for 5 h at 4°C to remove the unreacted PR that still has His-tag and residual TEV protease from the solution. The collected solution with Ni-NTA resin removed was the PR product with its His-tag removed.

Certain samples with enriched monomer or specific oligomeric species of PR were achieved by separation with an SEC after previous purification steps, as in other studies (10,11). PR was loaded on a HiLoad 16/600 Superdex 200 pg (GE Healthcare) connected to a Bio-Rad DuoFlow FPLC and was then run through the column by applying the 150 mM potassium chloride, 50 mM potassium phosphate dibasic buffer (pH 8.2) with 0.05% DDM at 0.5 mL/min. The collected protein fractions were concentrated using Amicon Ultra-15 Centrifuge Filter units with a 50 kDa cutoff limit (Millipore, Burlington, MA, USA) and the oligomeric state of each concentrated PR sample was later confirmed by gel electrophoresis measurements.

Preparation of PR-containing liposomes

Large unilamellar vesicles with desired composition were prepared by a lipid extrusion method. Lipid stocks dissolved in chloroform were purchased from Avanti Polar Lipids (Birmingham, AL, USA) and mixed to achieve a desired molar ratio between different lipid species. The lipid mixture was then dried under a nitrogen stream and further desiccated under vacuum overnight to ensure the removal of residue chloroform. The dried lipids were reconstituted with a HEPES buffer (10 mM HEPES, 150 mM NaCl [pH 6.7]), and lipid vesicles were extruded through the Avanti mini-extruder 19 times using filters with 200 nm pore size. The prepared lipid vesicles were then mixed with DDM surfactant solution to achieve a final DDM concentration 2 times the DDM critical micelle concentration (0.0088% [w/v]). The mixture was gently shaken for 1 h to form lipid-surfactant complexes, and the desired type of PR was then added to the mixture with a 1:50 PR-to-lipid molar ratio. The DDM surfactants in PR-lipid-DDM complex were then removed by using six vials of ~160 mg polystyrene BioBeads SM2 (Bio-Rad, Hercules, CA, USA) to drive the formation of PR liposomes.

SMA solubilization of PR

SMALP30010P was purchased from Orbiscope (the Netherlands). PR-expressing *E. coli* membranes, at a final concentration of 40 mg/mL, were incubated in 50 mM Tris-HCl, 10% glycerol, 300 mM NaCl, 2.5% (w/v) SMA (pH 8.0) for 20 h at 25°C with gentle rotation. Nonsolubilized material was sedimented at 100,000 $\times$ *g* for 1 h at 4°C to yield a supernatant containing PR-SMALP.

Native gel electrophoresis and western blotting

Blue native polyacrylamide gel electrophoresis (BN-PAGE) was performed using an XCell SureLock Mini-Cell apparatus with NativePAGE Bis-Tris Protein Gels having a 3–12% acrylamide gradient (Thermo Fisher, Waltham, MA, USA). PR sample preparation and gel electrophoresis were performed according to the instructions provided by the manufacturer. The destained gel was then imaged with a ChemiDoc MP imaging system (Bio-Rad) using the default protocol for Coomassie blue dyes. Western blotting of BN-PAGE was performed using an XCell II Blot Module by following the instructions for western blotting of NativePAGE Gels provided by the manufacturer. The blotted PVDF membrane was rinsed with deionized water and blocked in a TBST buffer containing 5% (w/v) dry milk. The immunodetection was then done by applying HRP-conjugated Anti-6X His tag antibody (Abcam, Cambridge, MA; ab1187) targeted to the six-histidine tag at the N-terminus of PR at 1:5000 in a TBST buffer containing 0.5% (w/v) milk. The membrane was then imaged with a ChemiDoc MP imaging system (Bio-Rad) using the default protocol for chemifluorescence dyes.

SDS-PAGE and PR cross-linking

Cross-linking of inter-PR lysines using the chemical cross-linkers DSG, DSS, or BSOCOES were performed similarly to as reported in the literature (39). A small volume of cross-linker in a freshly made 150 mM DMSO solution was added in large molar excess (20–100 times) relative to the amount of PR in the base phosphate buffer, quantified by optical absorption, such that the final DSS concentration was 2 mM. After incubation for 1 h at room temperature with gently mixing, the cross-linking reaction was quenched by addition of Tris to a final concentration of 50 mM. The same procedure was used to cross-link purified PR and PR in *E. coli* membranes extracted by ultracentrifugation (220,000 $\times$ *g*) after cell lysis.

SDS-PAGE was performed using a Bio-Rad electrophoresis apparatus with Criterion TGX Stain-Free gels having an 8–16% acrylamide gradient (Bio-Rad). Samples containing ~3 μg PR were incubated at 37°C for 30 min to 1 h with Laemmli buffer (final SDS concentration of 1%), and then centrifuged to remove the unsolubilized portions. The gel was run at 120 V for 1 h and imaged with a ChemiDoc MP imaging system (Bio-Rad) using a PR-specific protocol (excitation with green epi light and 695/705 filters to detect emission) based on the fluorescence properties of PR.172 protein markers (Precision Plus, Bio-Rad) and total proteins were further imaged using the Stain-Free protocol of ChemiDoc MP. Molecular weight estimates were calculated using the ImageLab software (Bio-Rad).

MD simulation on blue-light-absorbing PR oligomers in lipid bilayers

The x-ray crystal structures of blue-light absorbing PR (BPR) pentamer from HOT75 (PDB: 4KLY) and hexamer from Med12 (PDB: 4JQ6) were used as the starting structure. Each oligomer was inserted into a 1-palmitoyl-2-oleoyl-sn-glycero-3-phosphoethanolamine/1-palmitoyl-2-oleoyl-*sn*-glycero-3-phosphoglycerol (POPE/POPG) (3:1 molar ratio) bilayer using the replacement method of the CHARMM-GUI server (40–42), with a total of 827 and 808 lipids, respectively. After addition of water molecules and solvent ions (100 mM NaCl), the BPR lipid bilayer system had a total of 244,212 and 289,929 atoms for pentamer and hexamer, respectively. Two copies were generated for each oligomeric system for a total of four trajectories. All systems were equilibrated for >100 ns using a 2-fs timestep in the *NPT* ensemble ($p = 1$ atm, $T = 310$ K with the Nosé-Hoover barostat and thermostat) with NAMD 2.13 (43) based on CHARMM-GUI protocol with the CHARMM c36 force field for lipids, PR, and the retinal chromophore (44–48). After equilibration and estimation of the requisite boost potentials, Gaussian accelerated MD (GaMD) in NAMD (49) was run for >300 ns for the pentamer systems and >1000 ns for the hexamer systems. Analysis of GaMD results was carried out in VMD (50) and LOOS (51).

Continuous wave EPR measurement on spin labeled PR

The EPR probe, or MTSL spin label, was covalently linked to PR mutants with selected cysteine mutation sites as was introduced in a previous study

(10,11). In brief, PR with selected cysteine mutation sites were treated with 10× molar excess of MTSL spin label when it was bound on the Ni-NTA resin (Thermo Scientific). The unlabeled MTSL was then removed in later purification steps by either desalting or SEC processes. The prepared PR liposome sample with spin labels were studied with X-band (0.35 T) EPR measurements at room temperature using a Bruker (Billerica, MA, USA) EMXplus spectrometer. The continuous wave EPR spectra were taken under a setting of 20 mW microwave power, 1 G modulation amplitude, and 150 G total sweep width.

Optical absorption measurements and analyses

The UV-visible absorption spectra of PR under different conditions were taken using a Shimadzu UV-1800 spectrophotometer. All samples were prepared to have an optical density above 0.3 at 520 nm and an initial volume of 750 μL by diluting the PR sample stocks with the HEPES buffer mentioned above for lipid samples. For each PR sample, the optical absorbance between a wavelength range of 400–750 nm in increments of 0.5 nm were recorded under at least 20 different pH values that spread equally between pH 4 and 10. The pH of each sample was adjusted by titrating with 1 M NaOH (aq.) and 1 M HCl (aq.), and the pH was then measured by Orion Star A111 pH benchtop meter (Thermo Fisher Scientific, Waltham, MA, USA) equipped with an Orion ROSS Micro pH electrode before each optical absorption measurement. The pKa of PR D97 residue was determined by analyzing the pH-dependent optical absorption transition. The obtained optical absorption spectra under various pH conditions were processed by subtracting each absorption spectrum from the most basic one (pH ∼10). The differential absorbance at 570 nm, which supposed to be the wavelength that showed the greatest differential absorbance change, was normalized and fitted by the Henderson-Hasselbalch equation. The fitting was done by MATLAB (The Mathworks, Natick, MA) using home-built codes. The detail of the fitting algorithm and codes was published in our previous study (21).

The time-resolved UV-visible measurements were done using a SpectraPhysics Nd:YAG laser with a monochromator. PR samples were excited by a 532-nm pulse laser with 10 ns duration, and the PR transient absorbance under various wavelengths were monitored over a time span of 10 μs to 0.5 s by an oscilloscope. The fitting analyses on the transient spectra at 410 nm was done by MATLAB (The Mathworks) using home-built codes. The differential absorbance at 410 nm were assumed to be mainly contributed by the blue-shifted M intermediates, both M_1 and M_2 combined, as the absorbance of the other intermediates (e.g., K, N, PR, PR') is significantly lower at this wavelength (28). With this assumption, the growth and decay of the difference spectra at 410 nm represented the accumulation and decay of the M intermediates, respectively. A simplification was made by considering the reverse reactions of the K-M and M-N transitions to be negligible. As a result, a biexponential model for a simple first-order two-step consecutive reaction model (Fig. 3 *C*) could be used to fit the differential absorbance at 410 nm:

$$\Delta Abs_{410nm} = a\frac{k_1}{k_2 - k_1}\left(e^{-k_1 t} - e^{-k_2 t}\right),$$

where a was a parameter that reflected the magnitude of the differential absorbance, k_1 represented the rate constant of the K-M transition step, and k_2 represented the rate constant of the M-N transition step. The difference absorbance data at 410 nm from Fig. 3, *A* and *B* (*purple lines*) were fitted using the above reaction model (*smooth black curves*).

Cryo-EM sample preparation and data acquisition

For grid preparation, copper Quantifoil R2/1300 grids with a carbon foil were first glow-discharged for 30 s at 25 mA in the residual atmosphere using a GloQube Plus Glow Discharge System. Two microliters of purified 101 μM WT PR in DDM micelles were subsequently applied and incubated for 10 s at 4°C and 100% humidity before blotting for 3 s with a zero blot force and plunge frozen into liquid ethane using an FEI Vitrobot MkIV. During the entire freezing process the Vitrobot was covered in aluminum foil and a resting time of 10 s (compared with the ∼0.5 s photocycle of WT PR in DDM micelles) before blotting was added to prevent PR excitation and to limit the range of photocycle conformations in the sample. Micrographs were collected using a Titan Krios operated at 300 kV equipped with a Gatan BioQuantum energy filter operating over a calculated defocus range of −0.2 to −3.3 μm. A K3 detector operating in electron counting mode was used to record 27,398 micrographs at a pixel size of 0.68 Å^2 px^{-1} (corresponding to a nominal magnification of 1,650,00×) over a 4s exposure at a 15 e px^{-1} s^{-1} flux yielding a total fluence of 60 e px^{-1}, fractioned into 45 dose fractions.

Cryo-EM data processing

Preprocessing steps were performed with cryoSPARC Live v3.1.0 (52). First, motion-correction and dose-weighting was accomplished using MotionCor2 v2.1.1 (53). Contrast transfer function estimates for the motion-corrected micrographs were then calculated with CTFFIND4 v4.1.13 (54). Poor-quality micrographs were discarded. Following several rounds of 2D classification, 67,997 remaining particles were used for 3D classification.

RESULTS

PR exists as both hexamers and pentamers in *E. coli* membrane and synthetic liposomes

Although both hexameric and pentameric PR have been reported in various surfactant and reconstituted lipid environments (7,10,12,55–58), only hexamers have previously been observed in *E. coli* membranes (11), while Hirschi et al. reported on PR being primarily pentamers upon crystallization and when solubilized in cymal-5 micelles (57), and Maciejko et al. reported mainly on the pentamer population in DMPC/DMPA (9:1) liposomes (36). We performed BN-PAGE and western blot analyses of *E. coli* cell lysates containing PR-WT and found that both PR hexamers and pentamers are present but unresolved (Fig. S1). Since these two oligomeric species have slightly different spacing among the subunits, cross-linkers of various sizes were applied to PR-containing *E. coli* membranes to stabilize both species separately, with the goal to resolve the coexisting two oligomer populations. The proteins were cross-linked with either DSG, DSS, or BSOCOES, three lysine-specific cross-linkers presented in order of increasing length, followed by SDS-PAGE analysis. The spacer arm lengths (59) and the average attainable distances (60) of these cross-linkers are given in Table S1. As shown in Fig. 1, only PR hexamers were cross-linked by DSG and DSS, whereas BSOCOES stabilized both the hexameric and pentameric forms of PR. These results suggest that PR exists as both hexamers and pentamers in the native-like *E. coli* membrane. The pentamers were stabilized by only BSOCOES, likely because they possess a unique K125–K244 distance (21.2–21.9 Å according to MD simulations with Xwalk (61)), consistent with the accessible length of BSOCOES (average attainable distance: 21.6 Å) (see supplement 1 and Table S2). The K125–K244 cross-link is

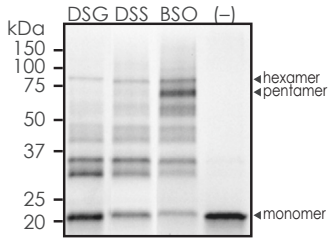

FIGURE 1 SDS-PAGE of WT PR cross-linked in extracted *E. coli* membranes using the three cross-linkers (lanes 1–3) and in membranes that have not been treated with cross-linker (lane 4). These cross-linked SDS-PAGE gels show monomer, dimer, trimer, tetramer, pentamer, and hexamer PR species. The emphasized monomer, pentamer, and hexamer species are labeled.

not present in the hexamer structures according to our MD simulations, hence no comparison could be made about the compactness in the overall structure of these two oligomeric states of PR.

Next, the oligomeric distribution of PR in synthetic liposomes was evaluated. POPC/POPG liposomes (4:1, mol/mol) were selected, as the anionic PG headgroup renders the membrane surface negatively charged, similar to that of the native bacterial membrane. PR in this composition has also been shown to be more uniformly oriented than in neutral bilayers (6), and to have increased active population as measured by a lower intrinsic pKa_{D97} (calculated from apparent pKa_{D97} by considering the local pH near the membrane surface according to the Gouy-Chapman model) compared with in POPC/DOTAP liposomes (20). BN-PAGE analysis again verified the coexistence of PR pentamers and hexamers in the POPC/POPG liposomes, as well as in DDM micelles (Fig. S2 *A*). This time, despite cross-linking of WT-PR with BSOCOES in POPC/POPG liposomes, SDS-PAGE could not resolve whether one or both oligomeric forms were present, unlike with cross-linked WT-PR in *E. coli* membrane (Fig. 1) or in DDM micelles (11). Interestingly, cross-linked PR oligomers were observed only at high protein/lipid ratios (Fig. S2 *B*), suggesting that the cross-linking reaction was unfavorable for PR oligomers in liposomes (62,63). The limited accessibility of the cross-linkers to the PR surface may be owing to the significantly greater thickness of the POPC/POPG membrane compared with the *E. coli* membranes, which would limit the accessible surface of PR to the solvent.

MD simulations were next used to evaluate the stability of the pentamer and hexamer assemblies of PR in different membrane environments. Systems with BPR crystal structures placed in a POPE/POPG (4:1, mol/mol) lipid bilayer for both the pentameric (PDB: 4KLY) and hexameric forms (PDB: 4JQ6) were equilibrated up to 100 ns, followed by several hundred ns of GaMD simulations (49). The stability of both oligomeric species was assessed via calculation of a packing score at each protomer-protomer interface (Fig. 2), defined as the relative degree of contact at a given interface. Higher packing scores correlate with greater interactions between monomers. Although both oligomeric forms of PR remained intact in the lipid bilayer environment during the GaMD simulations, different behaviors were observed between the hexamers and pentamers. The PR hexamer had much higher packing scores at four of the six interfaces compared with the pentamer, but the interfaces between protomers 3-4 and 6-1 were significantly less packed (Fig. 2 *B*, *top*). These two interfaces lie opposite one another, indicating that the hexamer could be formed via a dimer of trimers. In contrast, the interfaces of the pentamer had a much broader distribution of packing scores. Overall, these computational results suggested that a synthetic lipid bilayer environment facilitates assembly of stable PR in either oligomeric state, but that subtle differences exist between hexamers and pentamers.

We know that there are key oligomer interfacial contacts defined by specific interactions: the W34 to H75 hydrogen bond is maintained in both the pentameric and hexameric states, whereas the E50-R51-D52 salt bridge exists solely in the pentameric form, illustrated in Fig. 2 *A*. In addition, PR oligomers are further stabilized by nonspecific interactions. This is supported by the coexistence of multiple PR oligomer populations, including dimers, trimers, pentamers, and hexamers, and by the observation that the PR oligomer population is modulated by liposome composition and high salt concentrations that tend to alter nonspecific molecular interactions. Interestingly, a recently reported cryo-EM study of PR solubilized in Cymal-5 detergent micelles yielded a BN-PAGE analysis that revealed the presence of only pentamers of PR construct without a His-tag, and suggested that PR hexamers are formed only due to the presence of the His-tag added for purification purposes (57). In contrast, our BN-PAGE analysis of PR WT, upon removal of His-tag, revealed both pentamer and hexamer species in DDM micelles, in *E. coli* membranes, as well as in POPC/POPG liposomes (Fig. S3 *A*), ruling out a dominant contribution by the His-tag under the conditions investigated here. We have also performed a preliminary cryo-EM study of PR WT in DDM micelles (experimental details in materials and methods) and observe clear 2D and 3D classifications (Fig. S4) of the PR pentamer. Interestingly, we did not observe hexameric species of PR by cryo-EM. However, this does not mean that hexameric species do not exist. The PR sample consists of a heterogeneous population of oligomers (dimers, trimers, etc., besides pentamers) that likely is due to contributions from nonspecific interactions to stabilizing the oligomer interface. This heterogeneity makes PR oligomers inherently difficult to fully characterize by cryo-EM. The observed results still can mean that no stable hexamers are present, or that the hexamer makes up a more dynamic and heterogeneous assembly, and that the pentamer is the most stable and/or homogeneous population.

We next investigated whether PR oligomers are the product of nonspecific associations of PR molecules tightly

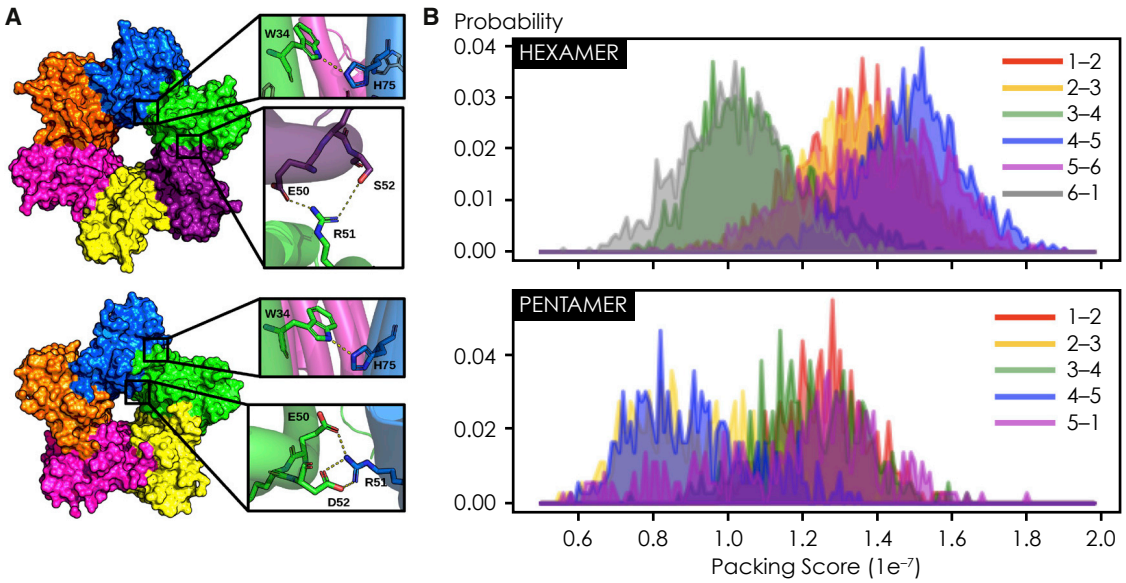

FIGURE 2 Molecular dynamics (MD) simulations on BPR crystal structures placed in a POPE/POPG (4:1, mol/mol) lipid bilayer. (*A*) PR hexamer and pentamer structures with numbering on each subunit to indicate the interface or intersubunit distances assessed by simulation. (*B*) Histogram of packing scores of BPR hexamers and pentamers at different oligomeric interfaces from GaMD simulations.

packed in a lipid membrane by decreasing the protein:lipid ratios, effectively diluting PR density in the proteoliposomes, and evaluating specific intermolecular interactions among PR oligomers by EPR lineshape analysis. In particular, the cross-protomer distance between residues 55 of PR has been known to be <16 Å, resulting in characteristic and distinct EPR line broadening (11). Our results showed that at protein/lipid ratios of both 1:30 and 1:100, the EPR spectra of PR spin-labeled at residue 55 exhibited the characteristic dipolar broadening seen in PR oligomers solubilized with DDM micelles (Fig. S3 *B*). This indicates that residues 55 are consistently near the cross-protomer interface of PR oligomers, and that PR oligomer formation is partially driven by specific cross-protomer interactions intrinsic to PR. Our results also suggest that nonspecific interactions from the His-tag or among PR molecules in close proximity are not a dominant factor in the formation of PR oligomers in synthetic liposomes, but that nonspecific interactions still do play a role in PR oligomer formation, giving rise to the heterogeneity of PR oligomer populations.

Oligomerization slows down the photocycle of PR in liposomes

We next sought to understand how oligomerization affects the proton transport function of PR in synthetic liposomes compared with PR in detergent micelles by evaluating the rate of proton transport. In detergent micelles, oligomerization has been demonstrated to slow down PR's proton transport two- to three-fold (11,21). To observe this process in POPC/POPG liposomes, we characterized the photocycle of the oligomer-dominant PR WT and of the monomer-enriched E50Q mutant (36). Compared with PR E50Q, the WT form exhibited differential absorbances that peaked at longer timescales at 410 nm (WT: ~500 μs; E50Q: ~200 μs) and at 590 nm (WT: ~4 ms; E50Q: ~2 ms) (Fig. 3). This result establishes that oligomerization slows down PR's accumulation of the *M* and *N* intermediates (28) in the liposome environments, as it did in the detergent micelle environment (11,21). Similar differences were also observed at 470, 500, 550, and 630 nm (Fig, S5, *A* and *B*), although the growth and decay of the transient absorbances at these wavelengths could not be attributed to specific photointermediates, due to overlap of different absorbances and low signal/noise ratio, particularly at 630 nm. Overall, the results reveal that oligomerization slows the kinetics of PR's photocycle in the liposome environment.

To quantify the extent to which oligomerization decreases the kinetics of the PR photocycle in liposomes compared with PR in detergent micelles, we performed a quantitative analysis of the transient absorbance data for WT PR and the E50Q mutant. The 410-nm traces, associated with the accumulation and decay of the *M* photointermediate, were fitted with a biexponential model (64) (see materials and methods). The results indicated that in liposomes, the *K-M* transition rate coefficient k_1 for the oligomer-dominant WT PR was ~2 times smaller than that for the monomer-enriched E50Q PR (WT: 8.7 ms^{-1}; E50Q: 16.9 ms^{-1}), while the *M-N* transition rate coefficient k_2 was ~4.5 times smaller (WT: 0.11 ms^{-1}; E50Q: 0.5 ms^{-1}). A very similar result was observed in the DDM detergent environment: the k_1 coefficient for oligomer WT PR was ~2 times smaller than that for E50Q PR (WT: 10.1 ms^{-1}; E50Q: 21.7 ms^{-1}), while the k_2 coefficient was ~4.5 times smaller (WT: 0.16 ms^{-1};

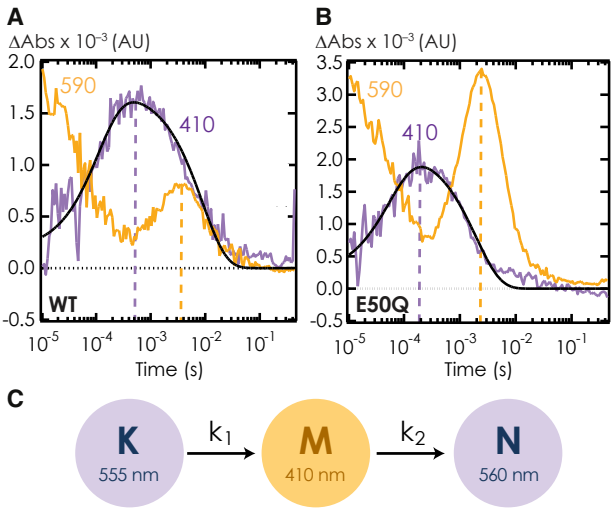

FIGURE 3 Transient difference absorbance data of (*A*) WT PR and (*B*) E50Q PR reconstituted in POPC/POPG (80:20, mol/mol) liposomes. Measurements were performed at pH 8.5 and ~293 K. The transient absorbance changes at 410 nm (*purple*) and 590 nm (*orange*) were collected after PR was photoactivated by a green-light pulse laser. The dashed vertical lines indicate the approximate timings for the transient absorbance at 410 and 590 nm to reach local maximum. Dark solid curves in (*A*) and (*B*) are the fitting curves of the 410 nm transient absorbance (*purple*) from oligomeric WT PR and monomer-enriched PR E50Q, respectively, using a first-order two-step consecutive reaction model illustrated in (*C*) to describe the accumulation and the decay of *M* intermediates in PR's photocycle.

E50Q: 0.77 ms^{-1}) (11,21) (Figs. S5, *C* and *D* and Table 1). Taken together, these results revealed that oligomerization, in both liposomes and detergent environments, slows PR photocycle kinetics in a significant and remarkably consistent manner, independent of the biomimetic host environments in which PR is embedded.

Effects of the liposome environments on PR's active population

In addition to the rate of the photocycle, the proton transport efficiency of PR is also affected by the population of active proteins, which can be assessed by measuring the apparent pKa of the key proton acceptor D97 (pKaD97) (29–32). In the detergent micelle environments, oligomerization was observed to raise PR's pKa_{D97} by almost one pH unit (oligomers: 6.5–6.7; monomers: 7.4–7.8; Fig. 4 *A* and Table 2), indicating a significant decrease in active protein population at neutral pH (11). To elucidate how oligomerization affects PR's pKa_{D97} in liposomes, we disrupted the critical cross-protomer W34-H75 interaction, which results in the destabilization of the protonated form of D97 (34–37), by the two mutations W34D (34) and E50Q (36). We then used SEC to isolate the WT dimers from the oligomeric population. We then compared the pKa_{D97} of the mutants, W34D and E50Q, and of the isolated WT dimers with that of PR WT oligomers. The E50Q mutation destabilized the PR oligomers and populated a mixture of smaller oligomers (Fig. S6 *A*), while W34D did not destabilize the PR oligomers, as expected (Fig. S6 *A*). Unlike in DDM detergent micelles (11), it was difficult to enrich just the monomers in liposomes, thus a mixture of PR dimers and monomers was characterized. Our studies of PR in DDM showed that the pKa_{D97} values of the mutants (E50Q: 7.2; W34D: 7.3; Fig. 4 *A*) were similar to that of the monomer population of PR WT (7.4), and much higher than the oligomeric population of PR WT (6.7) (11), as expected. However, for PR embedded in POPC/POPG liposomes, the pKa_{D97} values of these mutants (E50Q: 6.4; W34D: 6.6; Fig. 4 *B*) were comparable with that of PR WT oligomers (6.4) (Fig. 4 *B*). Likewise, PR WT dimers in POPC/POPG liposomes exhibited a similarly low pKa_{D97} value of 6.2 (Fig. 4 *B*). We also varied the protein/lipid ratio between 1:10, 1:30, and 1:100 to test whether the cross-protomer interactions stabilizing PR oligomers could be diluted in the presence of excess lipids; however, we found negligible changes in the pKa_{D97} (6.5–6.6) (Fig. S6 *B*). These results indicate that the liposome environment itself is sufficient to maintain an active population of PR independent of the cross-protomer modulation of D97.

We have shown that the different lipid membrane mimetic environments of liposomes and detergent micelles significantly impact the proton transport properties of PR. Next, we explored the functional impact of extracting PR directly from *E. coli* membranes by using SMALPs, a nanodisc system that has recently emerged to be a highly efficient lipid membrane mimetic. The use of SMALPs enables detergent-free isolation of transmembrane proteins and retention of their native lipid environment. As a result, SMA has been suggested to be superior to other membrane mimetics in maintaining protein function (16,65,66). Herein, the protein transport function of PR solubilized with SMALPs was characterized via pKa_{D97} measurements and photochemical reaction cycle experiments. The monomer-enriched E50Q mutant was used, as the oligomer-dominant PR WT could not be captured, possibly due to the limited size of the nanodiscs (see supplement 2). Our results showed that PR E50Q in SMALPs exhibited a remarkably high pKa_{D97} of 8.9 (Fig. 5 *A*). This is 1.5–2.5 pKa units higher than those of PR E50Q reconstituted in DDM (7.2) or in POPC/POPG (6.4) (Fig. 4), indicating that the majority of PR monomers are incapable of proton transport at neutral pH values in SMALPs. Note that the fitting was poor for the data at pH < 6 due to the instability of SMALPs in this pH range

TABLE 1 Rate coefficients of both the *K-M* transition (k_1) and the *M-N* transition (k_2) for PR in liposome vs. micellar environments from first-order two-step consecutive reaction model fitting

	WT		E50Q	
	k_1 (ms^{-1})	k_2 (ms^{-1})	k_1 (ms^{-1})	k_2 (ms^{-1})
POPC/POPG	8.7	0.11	16.9	0.5
DDM (11,21)	10.1	0.16	21.7	0.77

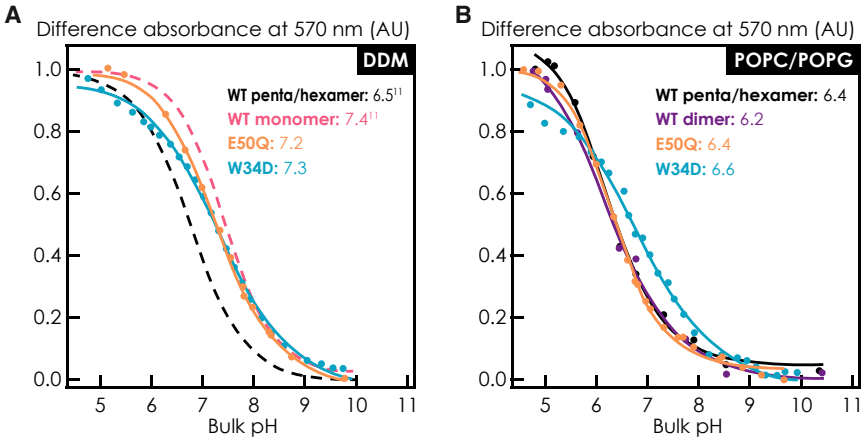

FIGURE 4 pH-dependent absorbance transitions at 570 nm and pKa_{D97} values for PR WT, E50Q, and W34D solubilized in (*A*) DDM detergent micelles and (*B*) POPC/POPG (4:1, mol/mol) liposomes. Previously published results are represented by dashed lines.

(67), which is in contrast to the high quality pKa_{D97} data of PR reconstituted in other membrane mimetics.

Next, time-resolved UV-vis light spectroscopy was used to evaluate the photocycle kinetics of PR E50Q in SMA at pH 8.0. We found that the photocycle kinetics were severely disrupted compared with PR in DDM micelles, exhibiting absorbances that rapidly diminished over time at all wavelengths examined (Fig. 5 *B*). The lack of movement at 410 nm indicates that the *M*-intermediate, characteristic of proton transport, is not observed. The gradual absorption decay observed at 550 and 590 nm is also nonnative as both wavelengths exhibit a complex photocycle in DDM micelles and liposomes. Such disruption of the PR photocycle could be explained by the very high pKa_{D97} of 8.9 for PR E50Q in SMALPs estimated above (Fig. 5 *A*). This indicates that the D97 residue is predominantly protonated, thereby interrupting the native *M*-*N* transition in the PR and effectively rendering most of the PR molecules inactive. This observation, however, persisted at pH 10.0 (Fig. 5 *B*), where the D97 residue should be deprotonated, indicating that the polymer nanodisc platform interferes with PR's photocycle kinetics beyond affecting the protonation state of D97. Taken together, SMALPs appear unable to maintain the proton transport capacity of PR, severely reduce its active population and disrupt its photocycle properties.

DISCUSSION

The key finding of this study is that oligomerization is a dominant factor that significantly decreases the kinetics of the PR photocycle. The oligomeric state of PR in *E. coli* membranes and synthetic liposomes are found to include both hexamers and pentamers (Figs. 1 and 2). In all cases, this study determined that oligomerization significantly slows down PR's photocycle in liposomes (Fig. 3) to a similar extent as previously shown for PR in micellar environments. This effect of oligomerization on the photocycle kinetics is likely owing to mechanical inhibition of key conformational changes.

At the same time we know from previous studies that the lipid-based membrane mimetic composition, regardless of the oligomeric state, exerts profound impacts on the active population of the receptor (20). This is further verified by the observation that disrupting the cross-protomer interaction that modulates the key proton acceptor D97 of PR did not decrease the active population of PR in liposomes (Fig. 4). In contrast to PR in the detergent DDM micelle environment, PR in liposomes was shown to maintain the active protein population harboring deprotonated D97 even in the absence of the critical cross-protomer W34-H75 contact (Fig. 4 and Table 2). This cross-protomer hydrogen bond serves to increase the tautomerization efficiency of H75 (34,36), such that H75 can form a hydrogen bond that stabilizes the deprotonated form of D97 (35). Therefore, there must exist a mechanism by which liposomes can keep D97 deprotonated without the hydrogen bond with H75. These observations are unique to PR embedded in liposomes, and have been proposed to arise from long-range stabilizing electrostatic interaction between lipid headgroups and internal PR residues across the liposome bilayer, further modulated by the presence of salt in the buffer solution (150 mM NaCl) (20). PR embedded in a bilayer membrane environment composed of charged and zwitterionic lipids can create a much stronger surface potential that could modulate key electrostatic interactions that may keep D97 deprotonated when PR is reconstituted in liposomes, effectively compensating for the disruption of the cross-protomer W34-H75 interaction.

Strikingly, solubilizing PR from its native *E. coli* using SMA nanodiscs does not preserve the pKa_{D97} of PR reconstituted in liposomes. Rather, the SMA nanodisc environment leads to a drastic increase in pKa_{D97} of PR E50Q compared with that in liposomes or micelles, and a severe disruption of PR's photocycle properties (Fig. 5). As the nanodiscs are formed, the maleic acid moiety must be deprotonated (68), which could cause an increase in the local proton concentration around residue D97. As a result, residue D97 could become dominantly protonated, leading to

TABLE 2 The pKa_{D97} of PR variants in DDM detergent and POPC/POPG (4:1, mol/mol)

	WT penta-/hexamer	WT dimer	WT monomer	E50Q	W34D
DDM	6.5[11]	–	7.4[11]	7.2	7.3
POPC/POPG	6.4	6.2	–	6.4	6.6

SMALPs retain PR's native-like membrane environment but disrupt proton transport function.

the accelerated decay in photocycle (Fig. 5 *B*). Indeed, a similar trend has been observed with other membrane proteins embedded in SMALPs. In the *Rubrobacter xylanophilus* rhodopsin RxR, the pKa of K209 has been shown to increase by 1.8 pH units in SMALPs compared with that in DDM (69). In addition, in the photoreceptor sensory rhodopsin II *Np*SRII of *Natronomonas pharaonic*, an accelerated decay of the *M* photointermediate was found due to the high local proton concentration induced by the maleic acid group of the SMA polymer (70). Taken together, these results suggest that the charged functional groups of SMALPs can have a dramatic, and potentially adverse, effect on the membrane protein function via adverse local electrostatic interactions. Hence, it is not a given that SMALP-reconstituted membrane proteins display more native-like function, even though PR is lifted out of its native *E. coli* lipid membrane environment.

Although appearing unimportant in maintaining PR's low pKa_{D97} in liposome environments, oligomerization exerts a substantial impact on PR's rates of proton transport in both detergent micelle and liposome environments (Fig. 3 and Table 1). This indicates that during the photochemical reaction, PR undergoes structural changes that can be modulated by oligomerization, yet unconnected to the protonation state of D97. Such structural changes may not be limited to any specific region of PR, as movements induced by the photocycle (shown to involve helices D–G (10,12,57,71–74)) occur in regions distinct from the oligomeric interfaces (constituted by helices A–C (10,12,57)). Indeed, by using MD simulations, a recent study has demonstrated that PR pentamers, compared with the monomeric form, exhibited increased rigidity of the overall structure of PR in a POPE/POPG lipid membrane (75). Increased overall rigidity of PR oligomers might be the structural basis of why PR's photocycle overall is slightly faster in liposomes than in detergent micelles, specifically the rate coefficients associated with the accumulation and decay of the *M* intermediate (Table 1). In addition, different rigidities might render PR pentamers and hexamers functionally dissimilar, as we have shown that PR hexamers have slightly stronger cross-protomer associations and are more compact compared with the pentamers (see Fig. 2 and supplement 3). Our study demonstrates that both oligomeric distribution and biomimetic composition can impact PR's functional properties via mechanisms beyond the protonation state of residue D97, underscoring the importance of resolving the structural evolution of PR in different membrane mimetics during activation in the future.

CONCLUSIONS

This study distinguishes and emphasizes the extensive impacts of biomimetic composition and oligomeric distribution on the functional properties of PR. The evidence supports the role(s) of electrostatic interactions from lipid-based membrane mimetics in maintaining the deprotonated state of PR's primary proton acceptor D97. In addition, oligomerization significantly and consistently slows PR's photocycle kinetics, highlighting the prominent functional role of oligomerization. The task remaining is to investigate the molecular mechanism by which various membrane mimetics modulate the composition-dependent pKa_{D97} of PR and the associated structural changes and their rates that are pertinent to PR's photochemical reaction induced by oligomerization. Also, the functional differences between the pentameric and hexameric forms of PR remain to be explored. This study focuses on PR, but the findings are

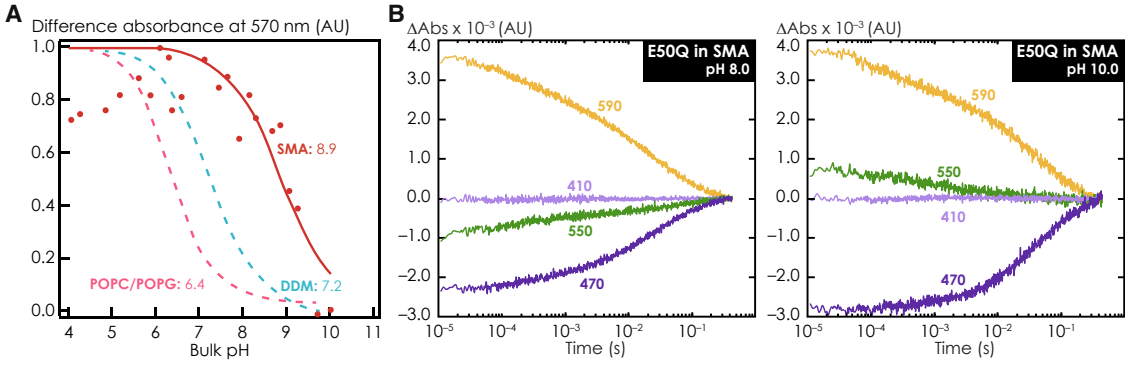

FIGURE 5 pH-dependent absorbance transitions of PR E50Q in SMALPs (*solid red line*) at 570 nm, compared with those of PR E50Q in DDM detergent micelles (*dashed blue line*) and in POPC/POPG liposomes (*dashed pink line*) (*A*) Transient absorbance data of PR E50Q extracted with SMALPs directly from *E. coli* membranes (*B*) Measurements were performed at pH 8.0 and 10.0 at ~293 K. The transient absorbance changes at 410, 470, 550, and 590 nm were collected after photoactivation of PR by a green-light pulse laser.

expected to be broadly applicable to other transmembrane proteins, reinforcing the importance of selecting the appropriate biomimetic platform for structure-function studies of these vital biomolecules.

SUPPORTING MATERIAL

Supporting material can be found online at https://doi.org/10.1016/j.bpj.2022.11.012.

AUTHOR CONTRIBUTIONS

C.-T.H., K.D.Q.N., M.W.B., S.H., A.K., M.N.I., B.F.C., B.M., and S.H. designed the research. C.-T.H., K.D.Q.N., M.W.B., S.H., A.K., M.K., M.N.I., N.B., E.C., E.A., M.R., and E.W. performed the research. C.-T.H., K.D.Q.N., M.W.B., S.H., A.K., M.R., and M.N.I. analyzed the data. C.-T.H., K.D.Q.N., M.W.B., S.H., B.F.C., B.M., and S.H. wrote the paper.

ACKNOWLEDGMENTS

The study of the functional impact of PR oligomerization was supported by the National Institute of General Medical Sciences of the National Institutes of Health under award number R35GM136411, the effect of membrane-mimetic environment on PR function by the Institute for Collaborative Biotechnologies through grant W911NF-19-2-0026 from the U.S. Army Research Office, and the study of PR function through protein dynamics by the National Science Foundation through grant MCB-1714888. Computational time was provided through West Virginia University's Research Computing and Extreme Science and Engineering Discovery Environment (XSEDE) allocation no. TG-MCB130040. The content is solely the responsibility of the authors and does not necessarily represent the official views of the U.S. government. We thank Prof. A. Amunts and Dr. V. Tobiasson for assistance with the cryo-EM analyses, which were conducted at the Cryo-EM Swedish National Facility which is funded by the Knut and Alice Wallenberg, Family Erling Persson and Kempe Foundations, SciLifeLab, Stockholm University, and Umeå University.

DECLARATION OF INTERESTS

The authors declare no competing interests.

REFERENCES

1. Lefkowitz, R. J. 2004. Historical review: a brief history and personal retrospective of seven-transmembrane receptors. *Trends Pharmacol. Sci.* 25:413–422.
2. Kaplan, J. H. 2002. Biochemistry of Na, K-ATPase. *Annu. Rev. Biochem.* 71:511–535.
3. Bragin, P. E., K. S. Mineev, and A. S. Arseniev. 2016. HER2 transmembrane domain dimerization coupled with self-association of membrane-embedded cytoplasmic juxtamembrane regions. *J. Mol. Biol.* 428:52–61.
4. Yan, N. 2017. A glimpse of membrane transport through structures—advances in the structural biology of the GLUT glucose transporters. *J. Mol. Biol.* 429:2710–2725.
5. Berndt, A., S. Y. Lee, and K. Deisseroth. 2016. Structural foundations of optogenetics: determinants of channelrhodopsin ion selectivity. *Proc. Natl. Acad. Sci. USA.* 113:822–829.
6. Wang, J., T. Albers, and C. Grewer. 2018. Energy landscape of the substrate translocation equilibrium of plasma-membrane glutamate transporters. *J. Phys. Chem. B.* 122:28–39.
7. Klyszejko, A. L., S. Shastri, and C. Glaubitz. 2008. Folding and assembly of proteorhodopsin. *J. Mol. Biol.* 376:35–41.
8. Schonenbach, N. S., M. D. Rieth, S. Han, and M. A. O'Malley. 2016. Adenosine A2a receptors form distinct oligomers in protein detergent complexes. *FEBS Lett.* 590:3295–3306.
9. Ferré, S., V. Casadó, and X. Guitart. 2014. Protein–Coupled receptor oligomerization revisited: functional and pharmacological perspectives. *Pharmacol. Rev.* 66:413–434.
10. Stone, K. M., J. Voska, and S. Han. 2013. Structural insight into proteorhodopsin oligomers. *Biophys. J.* 104:472–481.
11. Hussain, S., M. Kinnebrew, N. S. Schonenbach, E. Aye, and S. Han. 2015. Functional consequences of the oligomeric assembly of Proteorhodopsin. *J. Mol. Biol.* 427:1278–1290.
12. Edwards, D. T., T. Huber, and S. Han. 2014. Determining the oligomeric structure of proteorhodopsin by Gd3+-based pulsed dipolar spectroscopy of multiple distances. *Structure.* 22:1677–1686.
13. Jastrzebska, B., T. Maeda, and K. Palczewski. 2004. Functional characterization of rhodopsin monomers and dimers in detergents. *J. Biol. Chem.* 279:54663–54675.
14. Rietveld, A. W., and S. T. Ferreira. 1998. Kinetics and energetics of subunit dissociation/unfolding of TIM: the importance of oligomerization for conformational persistence and chemical stability of proteins †. *Biochemistry.* 37:933–937.
15. Schonenbach, N. S., S. Hussain, and M. A. O'Malley. 2015. Structure and function of G protein-coupled receptor oligomers: implications for drug discovery: studying GPCR Oligomer Function. *Wiley Interdiscip. Rev. Nanomed. Nanobiotechnol.* 7:408–427.
16. Gulati, S., M. Jamshad, and A. J. Rothnie. 2014. Detergent-free purification of ABC (ATP-binding-cassette) transporters. *Biochem. J.* 461:269–278.
17. Veatch, W., and L. Stryer. 1977. The dimeric nature of the gramicidin A transmembrane cbannel : conductance and fluorescence energy transfer stu of hybrid channels. *J. Mol. Biol.* 113:89–102.
18. Tunuguntla, R., M. Bangar, and A. Noy. 2013. Lipid bilayer composition can influence the orientation of proteorhodopsin in artificial membranes. *Biophys. J.* 105:1388–1396.
19. Lindholm, L., C. Ariöz, and A. Barth. 2015. Effect of lipid bilayer properties on the photocycle of green proteorhodopsin. *Biochim. Biophys. Acta.* 1847:698–708.
20. Han, C.-T., J. Song, T. Chan, C. Pruett, and S. Han. 2020. Electrostatic environment of proteorhodopsin affects the pKa of its buried primary proton acceptor. *Biophys. J.* 118:1838–1849.
21. Idso, M. N., N. R. Baxter, and S. Han. 2019. Proteorhodopsin function is primarily mediated by oligomerization in different micellar surfactant solutions. *J. Phys. Chem. B.* 123:4180–4192.
22. Lund, S., S. Orlowski, and J. V. Møller. 1989. Detergent structure and associated lipid as determinants in the stabilization of solubilized Ca2+-ATPase from sarcoplasmic reticulum. *J. Biol. Chem.* 264:4907–4915.
23. Rosevear, P., T. VanAken, J. Baxter, and S. Ferguson-Miller. 1980. Alkyl glycoside detergents: a simpler synthesis and their effects on kinetic and physical properties of cytochrome c oxidase. *Biochemistry.* 19:4108–4115.
24. Chawla, U., Y. Jiang, and H. Liang. 2016. A usual G-protein-coupled receptor in unusual membranes. *Angew. Chem., Int. Ed. Engl.* 55:588–592.
25. Brown, M. F. 2017. Soft matter in lipid–protein interactions. *Annu. Rev. Biophys.* 46:379–410.
26. Ranaghan, M. J., C. T. Schwall, N. N. Alder, and R. R. Birge. 2011. Green proteorhodopsin reconstituted into nanoscale phospholipid bilayers (nanodiscs) as photoactive monomers. *J. Am. Chem. Soc.* 133:18318–18327.

27. Váró, G., and J. K. Lanyi. 1991. Distortions in the photocycle of bacteriorhodopsin at moderate dehydration. *Biophys. J.* 59:313–322.
28. Váró, G., L. S. Brown, M. Lakatos, and J. K. Lanyi. 2003. Characterization of the photochemical reaction cycle of proteorhodopsin. *Biophys. J.* 84:1202–1207.
29. Dioumaev, A. K., L. S. Brown, and J. K. Lanyi. 2002. Proton transfers in the photochemical reaction cycle of proteorhodopsin. *Biochemistry.* 41:5348–5358.
30. Béjà, O., L. Aravind, and E. F. DeLong. 2000. Bacterial rhodopsin: evidence for a new type of phototrophy in the sea. *Science.* 289:1902–1906.
31. Dioumaev, A. K., J. M. Wang, Z. Bálint, G. Váró, and J. K. Lanyi. 2003. Proton transport by proteorhodopsin requires that the retinal schiff base counterion asp-97 Be anionic †. *Biochemistry.* 42:6582–6587.
32. Wang, W.-W., O. A. Sineshchekov, E. N. Spudich, and J. L. Spudich. 2003. Spectroscopic and photochemical characterization of a deep ocean proteorhodopsin. *J. Biol. Chem.* 278:33985–33991.
33. Ikeda, D., Y. Furutani, and H. Kandori. 2007. FTIR study of the retinal schiff base and internal water molecules of proteorhodopsin. *Biochemistry.* 46:5365–5373.
34. Ran, T., G. Ozorowski, and H. Luecke. 2013. Cross-protomer interaction with the photoactive site in oligomeric proteorhodopsin complexes. *Acta Crystallogr. D Biol. Crystallogr.* 69:1965–1980.
35. Hempelmann, F., S. Hölper, and C. Glaubitz. 2011. His75−Asp97 cluster in green proteorhodopsin. *J. Am. Chem. Soc.* 133:4645–4654.
36. Maciejko, J., M. Mehler, and C. Glaubitz. 2015. Visualizing specific cross-protomer interactions in the homo-oligomeric membrane protein proteorhodopsin by dynamic-nuclear-polarization-enhanced solid-state NMR. *J. Am. Chem. Soc.* 137:9032–9043.
37. Maciejko, J., J. Kaur, J. Becker-Baldus, and C. Glaubitz. 2019. Photocycle-dependent conformational changes in the proteorhodopsin cross-protomer Asp–His–Trp triad revealed by DNP-enhanced MAS-NMR. *Proc. Natl. Acad. Sci. USA.* 116:8342–8349.
38. Wang, W., and B. A. Malcolm. 1999. Two-stage PCR protocol allowing introduction of multiple mutations, deletions and insertions using QuikChangeTM site-directed mutagenesis. *Biotechniques.* 26:680–682.
39. Mattson, G., E. Conklin, and S. Morgensen. 1993. A practical approach to crosslinking. *Mol. Biol. Rep.* 17:167–183.
40. Jo, S., T. Kim, and W. Im. 2007. Automated builder and database of protein/membrane complexes for molecular dynamics simulations. *PLoS One.* 2, e880.
41. Jo, S., J. B. Lim, J. B. Klauda, and W. Im. 2009. CHARMM-GUI membrane builder for mixed bilayers and its application to yeast membranes. *Biophys. J.* 97:50–58.
42. Jo, S., T. Kim, V. G. Iyer, and W. Im. 2008. A web-based graphical user interface for CHARMM. *J. Comput. Chem.* 29:1859–1865.
43. Phillips, J. C., R. Braun, and K. Schulten. 2005. Scalable molecular dynamics with NAMD. *J. Comput. Chem.* 26:1781–1802.
44. Vanommeslaeghe, K., E. Hatcher, and A. D. Mackerell. 2009. CHARMM general force field: a force field for drug-like molecules compatible with the CHARMM all-atom additive biological force fields. *J. Comput. Chem.* https://doi.org/10.1002/jcc.21367.
45. Zhu, S., M. F. Brown, and S. E. Feller. 2013. Retinal conformation governs p K_a of protonated schiff base in rhodopsin activation. *J. Am. Chem. Soc.* 135:9391–9398.
46. Mertz, B., M. Lu, M. F. Brown, and S. E. Feller. 2011. Steric and electronic influences on the torsional energy landscape of retinal. *Biophys. J.* 101:L17–L19.
47. Klauda, J. B., R. M. Venable, and R. W. Pastor. 2010. Update of the CHARMM all-atom additive force field for lipids: validation on six lipid types. *J. Phys. Chem. B.* 114:7830–7843.
48. Nina, M., B. Roux, and J. C. Smith. 1995. Functional interactions in bacteriorhodopsin: a theoretical analysis of retinal hydrogen bonding with water. *Biophys. J.* 68:25–39.
49. Pang, Y. T., Y. Miao, Y. Wang, and J. A. McCammon. 2017. Gaussian accelerated molecular dynamics in NAMD. *J. Chem. Theor. Comput.* 13:9–19.
50. Humphrey, W., A. Dalke, and K. Schulten. 1996. VMD: visual molecular dynamics. *J. Mol. Graph.* 14:33–38, 27-28.
51. Romo, T. D., N. Leioatts, and A. Grossfield. 2014. Lightweight object oriented structure analysis: tools for building tools to analyze molecular dynamics simulations. *J. Comput. Chem.* 35:2305–2318.
52. Punjani, A., H. Zhang, and D. J. Fleet. 2020. Non-uniform refinement: adaptive regularization improves single-particle cryo-EM reconstruction. *Nat. Methods.* 17:1214–1221.
53. Zheng, S. Q., E. Palovcak, and D. A. Agard. 2017. MotionCor2: anisotropic correction of beam-induced motion for improved cryo-electron microscopy. *Nat. Methods.* 14:331–332.
54. Grant, T., A. Rohou, and N. Grigorieff. 2018. cisTEM, user-friendly software for single-particle image processing. *Elife.* 7, e35383.
55. Hoffmann, J., L. Aslimovska, and B. Brutschy. 2010. Studying the stoichiometries of membrane proteins by mass spectrometry: microbial rhodopsins and a potassium ion channel. *Phys. Chem. Chem. Phys.* 12:3480–3485.
56. Shastri, S., J. Vonck, and C. Glaubitz. 2007. Proteorhodopsin: characterisation of 2D crystals by electron microscopy and solid state NMR. *Biochim. Biophys. Acta.* 1768:3012–3019.
57. Hirschi, S., D. Kalbermatter, Z. Ucurum, and D. Fotiadis. 2020. Cryo-electron microscopic and X-ray crystallographic analysis of the light-driven proton pump proteorhodopsin reveals a pentameric assembly. *J. Struct. Biol. X.* 4, 100024.
58. Shibata, M., K. Inoue, and T. Uchihashi. 2018. Oligomeric states of microbial rhodopsins determined by high-speed atomic force microscopy and circular dichroic spectroscopy. *Sci. Rep.* 8:8262.
59. Double agents cross-linking reagents selection guide. (1999).
60. Green, N. S., E. Reisler, and K. N. Houk. 2001. Quantitative evaluation of the lengths of homobifunctional protein cross-linking reagents used as molecular rulers. *Protein Sci.* 10:1293–1304.
61. Kahraman, A., L. Malmström, and R. Aebersold. 2011. Xwalk: computing and visualizing distances in cross-linking experiments. *Bioinformatics.* 27:2163–2164.
62. Simons, K., and E. Ikonen. 1997. Functional rafts in cell membranes. *Nature.* 387:569–572.
63. Zeev-Ben-Mordehai, T., D. Vasishtan, C. A. Siebert, C. Whittle, and K. Grünewald. 2014. Extracellular vesicles: a platform for the structure determination of membrane proteins by cryo-EM. *Structure.* 22:1687–1692.
64. Tamogami, J., K. Sato, and N. Kamo. 2016. formation of M-like intermediates in proteorhodopsin in alkali solutions (pH $\geq$ ~8.5) where the proton release occurs first in contrast to the sequence at lower pH. *Biochemistry.* 55:1036–1048.
65. Knowles, T. J., R. Finka, and M. Overduin. 2009. Membrane proteins solubilized intact in lipid containing nanoparticles bounded by styrene maleic acid copolymer. *J. Am. Chem. Soc.* 131:7484–7485.
66. Jamshad, M., Y. P. Lin, and T. R. Dafforn. 2011. Surfactant-free purification of membrane proteins with intact native membrane environment. *Biochem. Soc. Trans.* 39:813–818.
67. Scheidelaar, S., M. C. Koorengevel, and J. A. Killian. 2016. Effect of polymer composition and pH on membrane solubilization by styrene-maleic acid copolymers. *Biophys. J.* 111:1974–1986.
68. Tonge, S. R., and B. J. Tighe. 2001. Responsive hydrophobically associating polymers: a review of structure and properties. *Adv. Drug Deliv. Rev.* 53:109–122.
69. Ueta, T., K. Kojima, and Y. Sudo. 2020. Applicability of styrene-maleic acid copolymer for two microbial rhodopsins, RxR and HsSRI. *Biophys. J.* 119:1760–1770.
70. Mosslehy, W., N. Voskoboynikova, and H. J. Steinhoff. 2019. Conformational dynamics of sensory rhodopsin II in nanolipoprotein and

styrene–maleic acid lipid particles. *Photochem. Photobiol.* 95:1195–1204.

71. Hirai, T., and S. Subramaniam. 2009. Protein conformational changes in the bacteriorhodopsin photocycle: comparison of findings from electron and X-ray crystallographic analyses. *PLoS One.* 4:e5769.

72. Hussain, S., J. M. Franck, and S. Han. 2013. Transmembrane protein activation refined by site-specific hydration dynamics. *Angew. Chem., Int. Ed. Engl.* 52:1953–1958.

73. Andersson, M., E. Malmerberg, and R. Neutze. 2009. Structural dynamics of light-driven proton pumps. *Structure.* 17:1265–1275.

74. Farrens, D. L., C. Altenbach, K. Yang, W. L. Hubbell, and H. G. Khorana. 1996. Requirement of rigid-body motion of transmembrane helices for light activation of rhodopsin. *Science.* 274:768–770.

75. Hirschi, S., D. Kalbermatter, Z. Ucurum, T. Lemmin, and D. Fotiadis. 2021. Cryo-EM structure and dynamics of the green-light absorbing proteorhodopsin. *Nat. Commun.* 12:4107.